nanomaterials

MDPI

Article

Effective Adsorption of Congo Red from Aqueous Solution Using Fe/Al Di-Metal Nanostructured Composite Synthesised from Fe(III) and Al(III) Recovered from Real Acid Mine Drainage

Khathutshelo Lilith Muedi [1], Vhahangwele Masindi [2,3], Johannes Philippus Maree [4], Nils Haneklaus [5,6] and Hendrik Gideon Brink [1,*]

[1] Department of Chemical Engineering, Faculty of Engineering, Built Environment and Information Technology, University of Pretoria, Pretoria 0028, South Africa; khathumuedi@gmail.com
[2] Magalies Water, Scientific Services, Research & Development Division, Erf 3475, Stoffberg Street, Brits 0250, South Africa; masindivhahangwele@gmail.com
[3] Department of Environmental Sciences, School of Agriculture and Environmental Sciences, University of South Africa (UNISA), P.O. Box 392, Florida 1710, South Africa
[4] ROC Water Technologies, P.O. Box 70075, Die Wilgers, Pretoria 0041, South Africa; maree.jannie@gmail.com
[5] Institute of Chemical Technology, Freiberg University of Mining and Technology, Leipziger Straße 29, 09599 Freiberg, Germany; nils-hendrik.haneklaus@extern.tu-freiberg.de
[6] Td Lab Sustainable Mineral Resources, University for Continuing Education Krems, Dr.-Karl-Dorrek-Straße 30, 3500 Krems, Austria
* Correspondence: deon.brink@up.ac.za; Tel.: +27-84-206-8338

check for updates

Citation: Muedi, K.L.; Masindi, V.; Maree, J.P.; Haneklaus, N.; Brink, H.G. Effective Adsorption of Congo Red from Aqueous Solution Using Fe/Al Di-Metal Nanostructured Composite Synthesised from Fe(III) and Al(III) Recovered from Real Acid Mine Drainage. *Nanomaterials* **2022**, *12*, 776. https://doi.org/10.3390/nano12050776

Academic Editor: Weiming Zhang

Received: 1 February 2022
Accepted: 23 February 2022
Published: 25 February 2022

Abstract: This study presents the first known exploration of Congo red dye (CR) adsorption by a polycationic Fe/Al Di-metal nanostructured composite (PDFe/Al) synthesised using Fe(III) and Al(III) recovered from authentic acid mine drainage (AMD). The PDFe/Al successfully removed CR from the aqueous solution. The mineralogical, microstructural, and chemical properties of the synthesised PDFe/Al adsorbent (before and after adsorption) were studied using state-of-the-art analytical instruments. The optimum conditions were observed to be 100 mg·L^{-1} CR, 1 g of the PDFe/Al in 500 mL adsorbate solution, 20 min of shaking, pH = 3–8, and a temperature of 35 °C. At optimised conditions, the PDFe/Al showed ≥99% removal efficacy for CR dye and an exceptionally high Langmuir adsorption capacity of 411 mg·g^{-1}. Furthermore, a diffusion-limited adsorption mechanism was observed, with two distinct surfaces involved in the adsorption of CR from an aqueous solution. It was determined that the adsorption of CR induced internal strain and deformation within the matrices and interlayers of the PDFe/Al which resulted in a marked increase in the adsorbent pore surface area and pore volume. The remarkably high adsorption capacity could be attributed to the high surface area. A regeneration study showed that the adsorbent could be reused more than four times for the adsorption of CR. The findings from this study demonstrated the feasibility of recovering valuable minerals from toxic and hazardous AMD and demonstrated their potential for the treatment of industrial wastewaters.

Keywords: acid mine drainage; Fe/Al di-metal composite; Congo red dye; adsorption modelling

1. Introduction

Environmental contamination by coloured, acidic, and metalliferous effluents has been an issue of topical concern globally [1,2]. This is fuelled by the magnitude of ecological and toxicological impacts posed by these wastewater streams to the receiving environment [3–5]. The problem of environmental contamination by coloured effluents, mainly from textile, pulp, paper, leather, and paint industries, is expected to grow primarily due to the rapid growth in population that will place proportional demand on resources to render goods

and services [1]. According to the literature, about 10–25% of dye materials used in the textiles, pulp and paper, food, leather, and painting industries are lost during the dyeing or coloring process [6]. On the other hand, acid mine drainage (AMD) is rich in toxic and hazardous chemicals that need to be removed before mine water can be discharged into the environment [7]. Furthermore, the problem of mine water is expected to prevail in the coming years [8,9]. For instance, South Africa alone produces close to 360 ML of AMD per year [10], and similar or greater volumes are expected in countries with heavy mining industries such as China, Canada, and Australia [11,12]. Henceforth, mining is inevitably expected to grow in many countries since it contributes to the gross domestic products (GDPs), job creation, and socio-economic development of any given country with good mineral endowments. Consequently, mining is indispensable for both developing and developed countries. The future mining prospects project that the generation of AMD will prevail into the future [13]. Be that as it may, stringent regulatory frameworks require AMD and dyed effluents, i.e., wastewater, to be treated prior to discharge into the environment [14,15]. This will enhance the integrity of the environment and its ability to foster life. Specifically, AMD comprises elevated levels of Fe (≈3000 mg/L), Mn (≈100 mg/L), Al (≈500 mg/L) and sulphates (≈12,000 mg/L) amongst traces of other toxic and hazardous contaminants [2]. High levels of Fe and sulphates make AMD a viable source of Fe- and S-based minerals [16,17]. Various studies have demonstrated the recovery of minerals from AMD and their potential beneficiations [11,18]. Akinwekomi et al. [17] demonstrated the recovery of Fe for the synthesis of goethite, hematite, and magnetite, whilst sulphate was recovered for the synthesis of gypsum and sulphuric acid [19]. These minerals have been beneficiated for different industrial applications with Fe-based minerals receiving notable attention in water treatment. This is mainly due to their magnificent affinity to anionic species such as phosphate [20], sulphates [21], arsenic [22], and anionic dyes [23], amongst others.

Due to its stellar tenacity, chemical stability, and strong adhesive properties, Congo red dye (CR) has been widely used in printing, clothing, pulp, textile, chemical, and paint industries [24]. The primary aim of dyeing is to impart colour and enhance the aesthetic value of the material being coloured. However, product water from these industries is rich in coloured effluents since only 80% of the dye is beneficially used [25]. According to the literature, dye-rich effluents give colour to the receiving environment, hence affecting their aesthetic values and physicochemical properties [26]. Furthermore, dyes are extremely persistent in the environment, which could be attributed to their non-biodegradable (bio-recalcitrant) nature [24,26]. Amongst a wide array of discovered dyes, CR has received paramount attention [27,28]. This is mainly attributed to its alarming degree of eco-toxicity. Epidemiological studies linked CR with allergies, dermatitis, eye, skin and gastrointestinal irritation, in addition to mutation, vomiting, and diarrhoea upon exposure [29–31]. In addition, the unique chemical properties of CR enable it to be metabolised to benzidine in the environment. Miandad et al. [32] explicitly linked benzidine to several forms of cancer and liver tumours for living organisms after chronic exposure. In addition, the presence of CR in water prevents the penetration of sunlight in the aqua-sphere, hence affecting benthic organisms, since this shading limits the solubility of gases. Poor light penetration further compromises the process of photosynthesis in aquatic flora, with deleterious effects on both flora and fauna in aqueous environments [24,33].

To counter toxicological effects, conform to regulatory requirements, and avert potential ecological degradations, a number of technologies have been developed for the removal of CR, including adsorption [34], precipitation [35], photocatalysis [36], filtration [37], bio-sorption [38], ion-exchange [39], and integrated approaches [40]. Worryingly, some technologies fail to attenuate CR, this is attributed to the fact that CR is a very stable organic compound that is intractable with respect to chemical or biological degradation and is also very resistant to oxidising agents, aerobic digestion, heat degradation, and light degradation [31,41]. Due to low associated costs, availability, and effectiveness, adsorption has been regarded as the foremost technology for the de-colouration of water, specifically

concerning CR [24,26]. For example, membrane technologies are effective but energy-intensive and require regular cleaning to regenerate the membranes. In addition, the cost associated with membrane fouling is very high, thus making the technology inaccessible for marginalised countries and communities [42]. Due to a high affinity for negatively charged chemical species, cationic metals (such as Fe(III) and Al(III)), double-layered hydroxides, and their nanocomposites have been widely employed for the removal of CR from aqueous solution, but the challenge is the use of virgin materials with the prospect of depletion in the coming years [6,23]. Ohemeng-Boahen et al. [6] reported the feasibility of using a chitosan/hematite nanocomposite hydrogel capsule fabricated via anionic surfactant gelation for the effective adsorption of CR from aqueous solution. Sriram et al. [43] successfully explored the application of Mg–Al-Layered Double Hydroxide (LDH) modified diatoms for the highly efficient removal of CR from aqueous solution. Dhal et al. [44] compared the use of ferrous oxalate, maghemite, and hematite nano-rods for the effective removal of CR dye from aqueous solution. The majority of these studies were using commercially sourced materials to synthesise the adsorbents which pose serious ecological challenges when these materials are depleted. As such, alternative ways to harvest metals such as Fe(III) and Al(III) could serve as the optimal method to preserve the environment, particularly when viewed within the circular economy context [22]. Consequently, this study seeks to recover Fe(III) and Al(III) from AMD for the synthesis of a nanostructured composite (PDFe/Al) and explore its efficacy for the removal of CR dye from aqueous solution. This is the first known study in design and execution to evaluate the feasibility of removing CR from aqueous solution using PDFe/Al synthesised from Al-Fe(III) recovered from real AMD. The findings from this study will go a long way in demonstrating the feasibility of recovering valuable minerals from toxic and hazardous mine drainage and valorise these for the effective removal of pollutants from aqueous solutions.

2. Materials and Methods

2.1. Feedstock and Sample Collection

Raw AMD was collected from a coal mine in the Mpumalanga Province of South Africa. All chemicals were purchased from Sigma-Aldrich (Darmstadt, Germany) and used as obtained without any further purification: potassium dichromate salt ($K_2Cr_2O_7$), caustic soda (NaOH), sulphuric acid (98.5% H_2SO_4), and hydrochloric acid (37% HCl). CR dye stock solution was prepared using CR dye powder. Aqueous samples and solutions were prepared using ultrapure water (18.2 MΩ-cm) prepared using an Elga PURELAB® Flex (ELGA LabWater, High Wycombe, UK). Experimental glassware was carefully and thoroughly cleaned before and after every use to avoid contamination.

2.2. Synthesis of PDFe/Al from AMD

The synthesis of PDFe/Al followed the same method as previously described [15]. To preferentially precipitate Fe(III) and Al(III) as (oxy)hydroxides, a known amount of AMD was diluted with NaOH until pH = 4.5 was measured. An overhead stirrer was used to agitate the mixture for 60 min at room temperature. The mixture was gently heated to 100 °C. with continuous stirring once the precipitation process was equilibrated. After the reaction vessel was heated and subsequently allowed to cool to room temperature, the precipitate was vacuum filtered and dried using Whatman® Grade 40 ashless filter paper (Whatman PLC, Maidstone, UK). The recovered material was then crushed into a fine powder in a vibrating ball mill () at 700 rpm before being calcined at 800 °C. The samples were then sieved through a 32 µm perforated sieve () to obtain the necessary particle size, and they were stored in a plastic "zip-lock" bag to preserve them from the environment until they were used

2.3. Preparation of CR Dye Stock Solutions

An amount of 1 g of CR dye was dissolved in 1 L ultrapure water (18.2 M-cm) to make 1000 mg·L^{-1}. The stock solution was made in a 1000 mL volumetric flask that had been

filled to the specified level. For each adsorption experiment, fresh aqueous solutions were made from the stock solutions.

2.4. Batch Experiments

A batch-experimental approach was adopted for the removal of CR dye from aqueous solutions using the synthesised PDFe/Al. Different parameters were studied for the adsorption of CR dye, such as initial concentration, adsorbent dosage, agitation time, temperature, and initial solution pH, where 500 mL of the CR dye solution was loaded in individual volumetric flasks. For quality control and quality assurance, all experiments were conducted in triplicate and the data were reported as means. The effects of the different parameters on the adsorption process were studied as summarised in Table 1.

Table 1. Studied parameters for CR dye adsorption using PDFe/Al.

Experiment No	Initial Concentration (mg·L^{-1})	Initial pH	Adsorbent Dosage * (g)	Agitation Time (min)	Temperature (°C)
1	1; 5; 10; 20; 30; 40; 50; 100; 150; 200	6–7	1	30	25
2	10	2, 3, 4, 5, 6, 7, 8, 9, 10 (±0.2)	1	30	25
3	10	6–7	0.1; 0.5; 1; 2; 3; 4; 5 (±0.0005)	30	25
4	10	6–7	1	1; 5; 10; 15; 20; 25; 30; 40; 50; 60	25
5	10	6–7	1	30	25; 35; 45; 55; 65

* Dispersed in a 500 mL batch reactor.

As depicted in Table 1, the effect of the initial CR concentration (1–200 mg·L^{-1}) on the adsorption process was studied by preparing fresh aqueous solutions from concentrated 1000 mg·L^{-1} CR dye stock solutions. The effect of PDFe/Al dosage on CR dye adsorption was studied by varying different dosages of the adsorbent (0.1–5 g) and agitating them with the respective adsorbate solutions. The effect of agitation time was studied by conducting the batch adsorption experiments for CR dye adsorption for different time intervals (1–60 min). The effect of initial solution pH was studied by adjusting the pH of CR dye solutions with 0.1 M NaOH and/or 0.1 HNO_3 to a desirable level (pH of 2–10). The effect of temperature was studied by conducting the batch adsorption experiments in a thermal shaker/incubator under different temperatures (25–65 °C). Concentrations of CR dye were analysed before and after the experiments.

To control for potential spectrophotometric interference resulting from the adsorbent matrix, the adsorbent was agitated in 500 mL distilled water overnight and, after the removal of the adsorbent, the eluent was analysed spectrophotometrically. No quantifiable change to the medium was measurable and, therefore, it was concluded that the adsorbent matrix would not cause spectrophotometric interference during the experiment.

2.5. Characterisation of Aqueous Samples

The pH levels of the aqueous solutions were measured using a Thermo ScientificTM Orion 3 Star portable pH meter before and after the adsorption experiments (Thermo Scientific, Waltham, MA, USA). A Mettler Toledo (Mettler Toledo®, Columbus, OH, USA) FiveGo EC/TDS/Salt/Temperature portable multimeter was used to measure electrical conductivity (EC), total dissolved solids (TDS), and salinity. The absorbance of the CR dye was measured using a WPA Lightwave II UV/Visible spectrophotometer (Labotec, Johannesburg, South Africa).

2.6. Characterisation of Solid Samples

X-ray diffraction (XRD) was used to determine the mineralogical composition and pattern of the Fe/Al and residual products, which was recorded using a Panalytical X'Pert PRO (Malvern Panalytical, Malvern, UK) equipped with a Cu-K radiation source. The Origin 2021b software program was used to deconvolute the XRD signal peak (OriginLab, Northampton, MA, USA). High-resolution scanning electron micrographs (HR-SEM-EDX)

were used to examine the surface morphology and composition of solid materials (Carl Zeiss Sigma VP FE-SEM with Oxford EDX Sputtering System, Carl Zeiss AG, Oberkochen, Germany). A Perkin-Elmer Spectrum 100 Fourier Transform Infrared Spectrometer (FTIR) with a Perkin-Elmer Precisely Universal Attenuated Total Reflectance (ATR) sampler was used to examine the metal functional groups in solid samples (Perkin-Elmer®, Waltham, MA, USA). The synthesised PDFe/Al and subsequent residues' Brunauer–Emmet–Teller (BET) surface area and BJH pore size were determined using BET equipment and a Micromeritics VacPrep 061 degassing system (Micromeritics Tristar II 3020, Micromeritics Instrument Corp., Ottawa, ON, Canada). The thermal stabilities of the synthesised PDFe/Al and residual products were determined using a Thermo Gravimetric Analyser (TGA) (SelectScience TGA Q500, TA instruments, Bath, UK) in ambient air at a flow rate of 50 mL·min^{-1} and a heating rate of 10 C·min^{-1}.

2.7. Point of Zero Charge (PZC)

The Smiiklas method [20] was used to determine the point of zero charge (PZC) of the synthesised PDFe/Al. In nine separate flasks, 50 mL of 0.1 M KNO3 solution was loaded. Using 0.1 M HNO3 and/or NaOH, the pH levels of the solutions were adjusted to 2–10. After that, each flask received 0.1 g of synthesised PDFe/Al, and the mixtures were allowed to equilibrate for 24 h at 25 °C. The pH of the filtrates was then measured after the PDFe/Al suspensions were filtered.

2.8. Adsorption Capacity and Removal Efficiency

2.8.1. Adsorption Capacity

Equation (1) was used to evaluate the adsorption capabilities of PDFe/Al for the removal of CR dye from aqueous solutions:

$$Q_e = \frac{(C_0 - C_e) \cdot V}{m} \quad (1)$$

where Q_e (mg·g^{-1}) is the adsorption capacity, C_0 (mg·L^{-1}) is the starting concentration of CR dye, C_e (mg·L^{-1}) is the equilibrium concentration of CR dye, V (L) is the volume of the CR dye solution, and m (g) is the dosage of PDFe/Al, respectively.

2.8.2. Removal Efficiency

Equation (2) was used to calculate the elimination effectiveness of CR dye by PDFe/Al:

$$\%R_e = \frac{(C_0 - C_e)}{C_0} \times 100 \quad (2)$$

where per cent R_e denotes the PDFe/Al removal effectiveness, C_0 denotes the initial CR dye concentration (mg·L^{-1}), and C_e denotes the equilibrium CR dye concentration (mg·L^{-1}).

2.9. Desorption Study

An approach described by Kumari et al. [21] was used to investigate the regeneration of PDFe/Al. An amount of 1 g of PDFe/Al was combined with 250 mL of 150 mg·L^{-1} CR dye solution in a 250 mL Erlenmeyer flask for 90 min in a batch experiment. After equilibration, the residue was centrifuged to separate it from the supernatant. To eliminate excess CR dye ions, the recovered residual material was washed five times with 250 mL of ultrapure water and dried. After that, 250 mL of 0.1 M HNO_3 was added to the dried sample at room temperature. The HNO_3 extract that resulted was collected and analysed for CR dye ions. Equation (3) was used to calculate the regeneration percentage:

$$\%Desorption = \frac{C_{des}}{C_0} \times 100 \quad (3)$$

where C_{des} (mg·L^{-1}) is the concentration of CR dye ions in the desorption eluent and C_0 (mg·L^{-1}) is the initial concentration of CR dye ions.

3. Results

3.1. Characterisation of PDFe/Al before and after CR Dye Adsorption

3.1.1. FTIR Functional Groups

A Fourier Transform Infrared Spectrometer (FTIR) was used to characterise the functional groups of the synthesised PDFe/Al before and after CR dye adsorption, as shown in Figure 1.

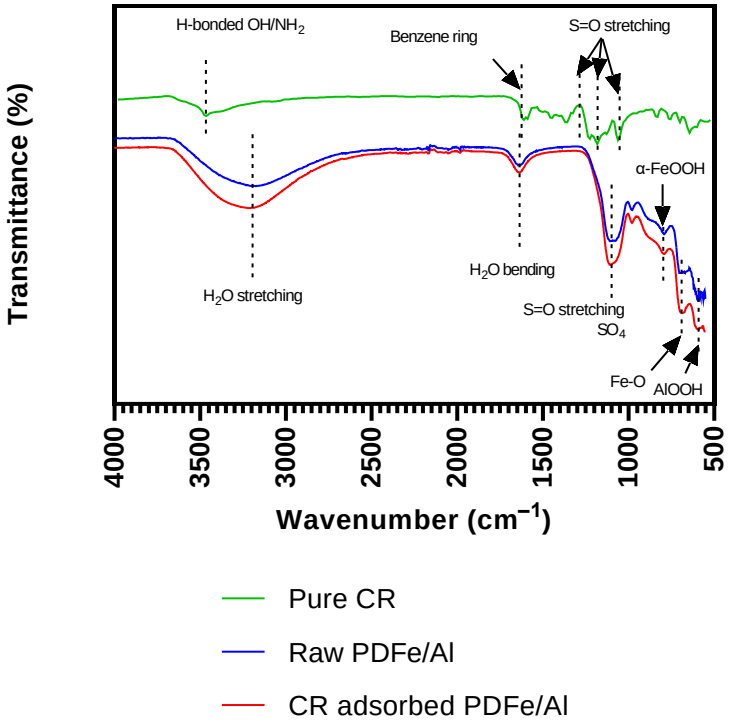

Figure 1. Functional groups of the synthesised PDFe/Al before and after CR dye adsorption.

As depicted in Figure 1, the transmittance bands of the synthesised PDFe/Al are shown before and after CR dye adsorption, as well as the FTIR spectrum of pure CR dye. For the raw and CR-adsorbed PDFe/Al, the high stretching of the –OH group is observed between 4000 and 3500 cm^{-1}, while at 1668 cm^{-1}, HOH stretching is observed [45]. Further on, as an attestation of CR dye adsorption, an increase in the sharp peak at 1134 cm^{-1}, likely an indication of S=O- stretching, is observed. S=O- was also observed in the spectrum for the pure CR at 1278, 1177, and 1041 cm^{-1} [46]. A small waveband is observed at 866 cm^{-1}, which could be an indication of –OH stretching in α-FeOOH [47]. Furthermore, the stretching of the Fe–O band is observed at 789 cm^{-1} The wavebands at 3740 and 2966 cm^{-1} could also indicate the stretching of the –OH group. The AlOOH band is observed to have stretched at 630 cm^{-1} [48].

3.1.2. XRD Mineralogical Composition

X-ray diffraction (XRD) was used to characterise the mineralogical composition of the synthesised PDFe/Al before and after CR dye adsorption, as shown in Figure 2.

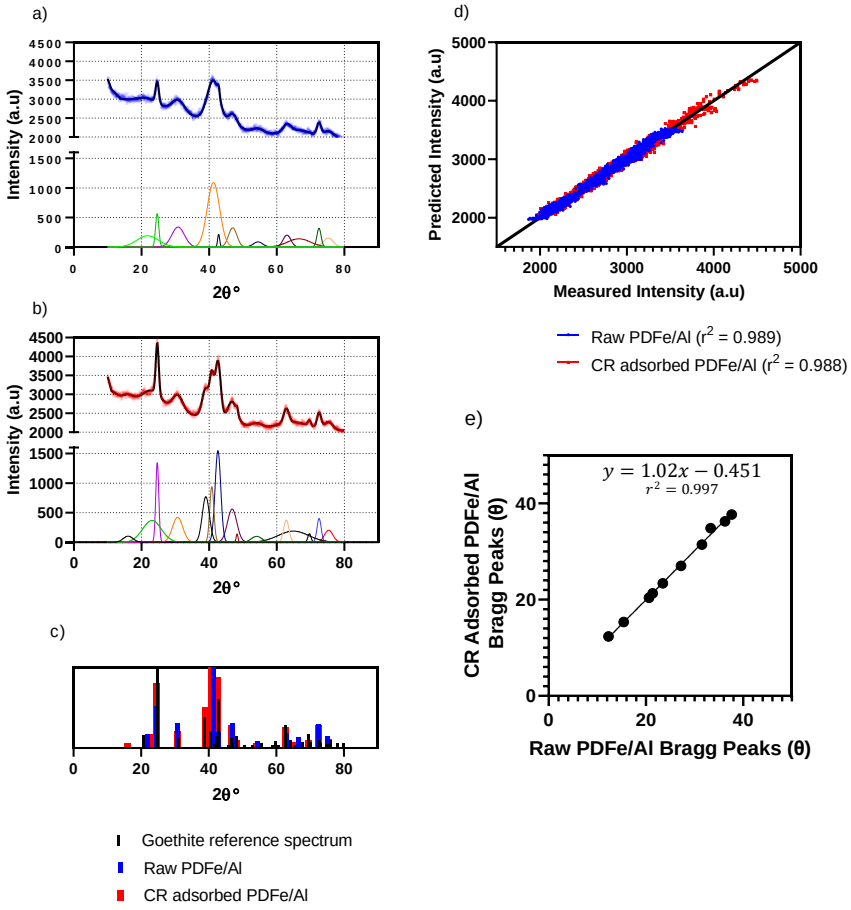

Figure 2. XRD analysis of the PDFe/Al composite (**a**) before and after (**b**) CR dye adsorption. The coloured peaks represent the deconvoluted peaks extracted from the XRD data (blue data in (**a**) and red data in (**b**)) with offset subtracted. (**c**) The relative peaks from (**a**,**b**) against the reference spectrum for goethite [22], indicating the positive characterisation of goethite in the sample. (**d**) The parity plot of the experimental data obtained from the XRD diffractometer and the fitted Gaussian peaks shown in (**a**,**b**), demonstrating the quality of the fitted curves. (**e**) Plot of the Bragg peak positions for (**a**) against the corresponding peaks in (**b**). The plot shows that a constant shift of -0.451° was measured after CR adsorption as compared to the raw PDFe/Al.

As illustrated in Figure 2, the XRD spectra of the PDFe/Al composite before and after CR dye adsorption are shown. It was observed that the XRD spectra depict the characteristic peaks for goethite—see Figure 2c—before and after adsorption, positively identifying the crystalline stricture as goethite [22]. The material also shows additional amorphous peaks after CR dye adsorption. Crystalline structures are observed to have formed at the surface of the material. The diffraction peaks between $2\theta = 20^\circ$ and $2\theta = 40^\circ$ show that the adsorption of CR dye occurred as observed from the peak size when compared to raw PDFe/Al.

From the relative positions of the fitted Gaussian peaks—shown in Figure 2a,b—as shown in Figure 2e, it can be concluded that a constant shift of -0.451° for the Bragg peaks after CR adsorption was observed. This is consistent with the significant adsorption strain experienced by the adsorbent during the adsorption of CR. According to Dolino et al. [49], the lattice mismatch parameter ($\Delta a/a$) in the direction perpendicular to the sample surface is directly proportional to the shift of the Bragg peak angle ($\Delta\theta$), according to the equation $\Delta a/a = \Delta\theta\cot\theta$. This equation shows that a shift in the Bragg peak would result in a proportional shift in the lattice mismatch parameter, which indicates strain within the crystal lattice [49,50]. The strains within the pore structures are likely a result of competition between expansion due to decreased surface energy and contraction due to

dispersion forces. These adsorption-induced strains result in the deformation of the pore structure of the adsorbent—mainly in the less rigid parts of the structure [49–51].

3.1.3. SEM Morphology

Scanning electron microscopy (SEM) was used to characterise the morphology of the synthesised PDFe/Al before and after CR adsorption, as shown in Figure 3.

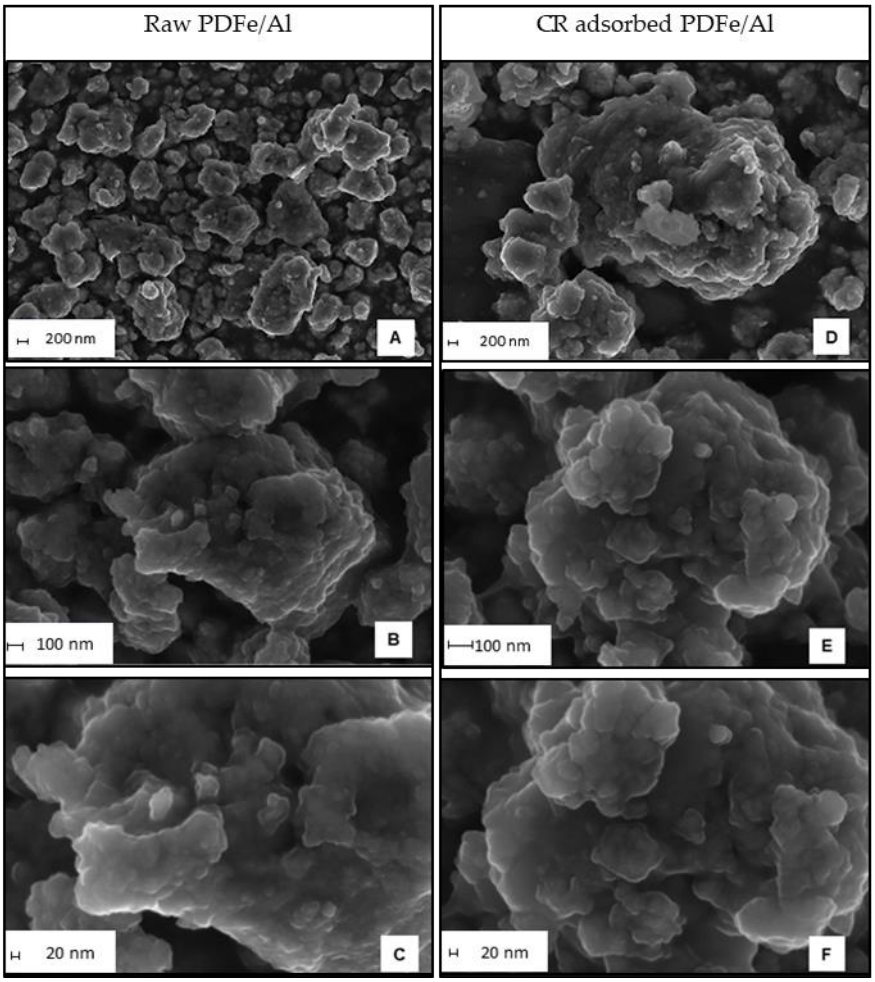

Figure 3. Morphology of the synthesised PDFe/Al before adsorption (**A**–**C**) and after CR dye (**D**–**F**) adsorption. The scale bars are shown in the bottom left of the figures.

As illustrated in Figure 3, the morphological properties of the synthesised PDFe/Al composite before and after CR dye adsorption is shown. Figure 3A–C illustrate the morphology of raw PDFe/Al composites at different sizes, where non-uniform pressed-like structures of irregular agglomerates are unevenly distributed. Figure 3D–F illustrates the morphology of the PDFe/Al composite after CR dye adsorption at different sizes, where protruding plateau-like structures and small spherical structures after contacting CR-rich water can be observed.

3.1.4. EDX Elemental Mapping

An energy dispersive X-ray (EDX) was used to characterise the mapping of the elemental composition of the synthesised PDFe/Al before and after CR adsorption, as shown in Figure 4.

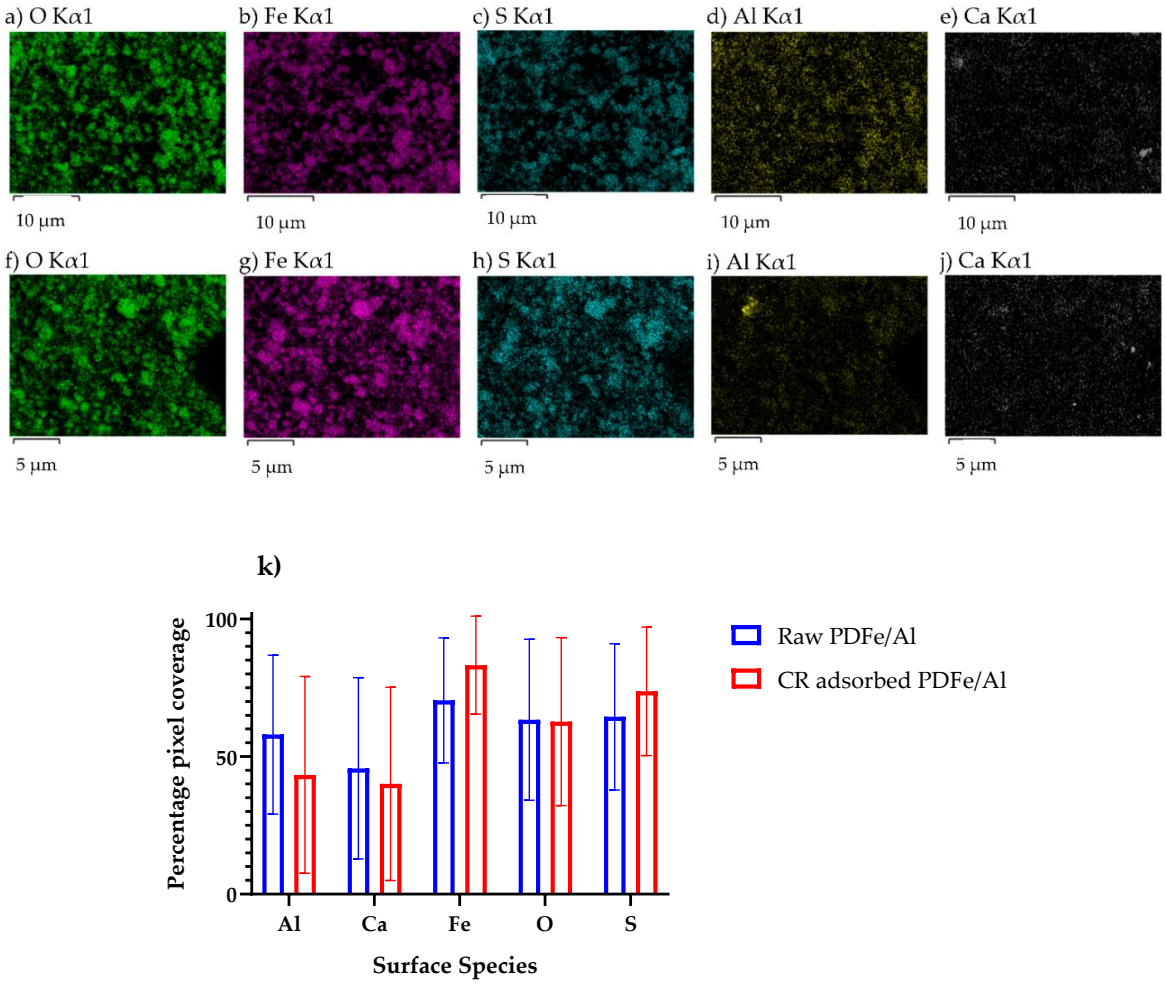

Figure 4. (**a**–**e**) Mapping of the elemental composition of the synthesised PDFe/Al before adsorption. (**f**–**j**) Mapping of the elemental composition of the synthesised PDFe/Al after CR adsorption. (**k**) The percentage pixel coverage of respective elements from EDX mapping. Error bars show standard deviations.

As illustrated in Figure 4, the elemental mapping of PDFe/Al dimetal composite before and after CR dye adsorption is shown. Figure 4a–e shows that the raw PDFe/Al dimetal composite exhibited the presence of both Fe and Al, hence confirmation of co-precipitation from AMD. The presence of S and Ca are a result of the presence of these minerals in the raw AMD. Figure 4f–j shows the elemental distribution of PDFe/Al dimetal composite after CR dye adsorption. Figure 4k was generated by comparing the respective pictures in Figure 4a–j with a pure black picture, using the method described previously [22]. The quantitative analyses in Figure 4k show that no significant change in the surface coverage for the different species before and after CR adsorption was discernable—this was confirmed by Student's t-test at the 5% significance level with t-statistics in excess of 35% for all surface species indicating that no significant difference between the surface coverage for the different species could be observed.

3.1.5. TGA Thermal Stability

Thermo-gravimetric analysis (TGA) was used to determine the thermal stability of the synthesised PDFe/Al before and after CR adsorption, as shown in Figure 5.

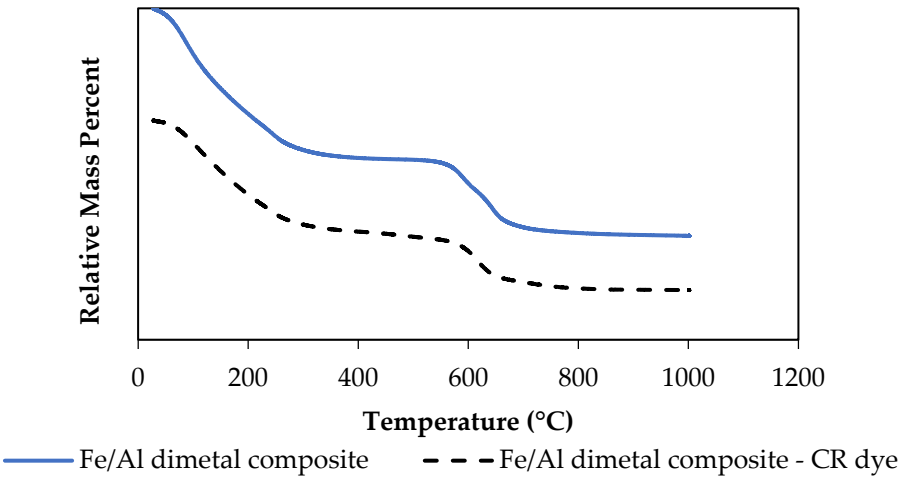

Figure 5. Thermal stability of the synthesised PDFe/Al before and after CR dye adsorption.

As illustrated in Figure 5, the thermal stability of PDFe/Al before and after CR dye adsorption is shown. The graphical results show that the calcination process occurred in three phases, where the first stage involves the loss of moisture from the material between 100 and 350 °C. The second stage involves the loss of HOH that is chemically bound to the material at 400–550 °C, while the third stage involves the loss of the hydroxyl group (–OH) at temperature >550 °C [22].

3.1.6. BET Surface Area and Porosity

BET surface area analysis was used to determine the surface area and porosity properties of PDFe/Al before and after CR dye adsorption, as illustrated in Figure 6 and Table 2.

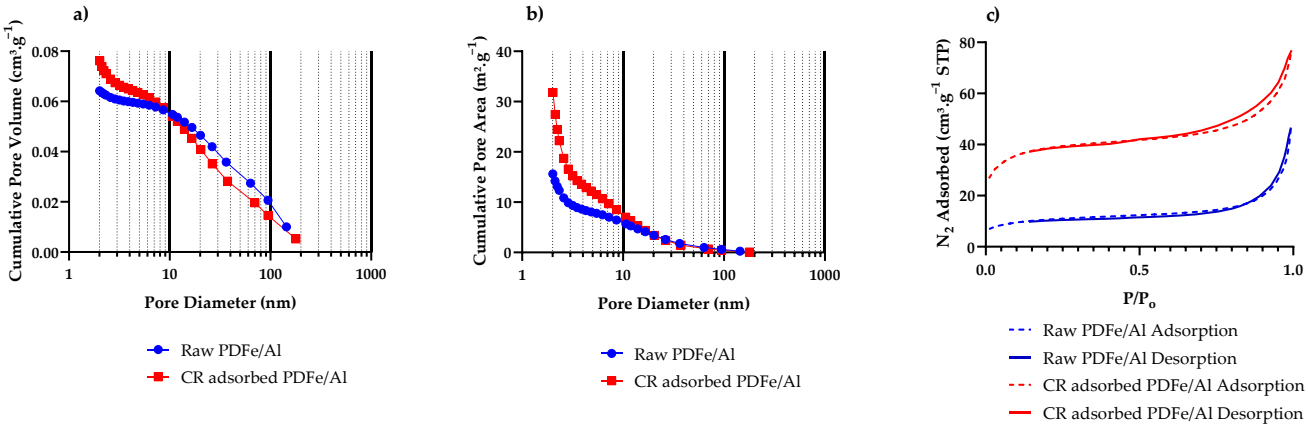

Figure 6. BET surface area and porosity analysis of PDFe/Al before and after CR dye adsorption. (**a**) The pore volume distribution, (**b**) the pore area distribution, and (**c**) the N_2 adsorption hysteresis loops for raw and CR-adsorbed PDFe/Al.

Table 2. Surface area and porosity properties of PDFe/Al before and after CR dye adsorption.

Parameter	Raw PDFe/Al	CR-PDFe/Al
BET Surface Area ($m^2 \cdot g^{-1}$)	37.58 ± 0.37	134.46 ± 2.06
Micropore Area (from t-Plot) ($m^2 \cdot g^{-1}$)	13.67	51.85
Pore volume (<179 nm) ($cm^3 \cdot g^{-1}$)	0.0621	0.1137
Micropore Volume ($cm^3 \cdot g^{-1}$)	0.0031	0.0155
BJH average pore diameter (nm)	16.47	9.58

As illustrated in Table 2, BET analysis was used to characterise the surface area and porosity properties of the PDFe/Al composite. It was observed that the adsorbent showed a massive increase in the surface area of approximately 37 $m^2.g^{-1}$ to 134 $m^2.g^{-1}$. Further analysis of the pore volume (Figure 6a) and area (Figure 6b) distributions show large spikes in both volume and area in the range pore diameters <20 nm when comparing the raw PDFe/Al composite to the CR-adsorbed material. In addition, the hysteresis loops for both raw and CR-adsorbed PDFe/Al (Figure 6c) show H4-type hysteresis behaviour, which is associated with slit-like pores [52]. Li et al. [53] reported that C, H, O, Na, Al, and Fe are atoms that can play a significant role in strengthening the Van der Waals forces of the material. The adsorption of CR dye, which contains C, H, O, and Na, causes significant changes in the internal forces within the material. These results are consistent with Figure 2e, which shows a significant adsorption-related strain within the adsorbent, resulting in the significant deformation of the materials [51]. Consequently, nanosized cracks form within the materials, which increases the internal pore volume, the micropore volume, and the micropore area (see Table 2). These cracks are then exhibited as slit-like pores, giving the characteristic H4-type hysteresis loop (Figure 6c) [52], which results in a corresponding increase in the adsorption capacity of the material due to an increased surface area available for adsorption [27].

3.2. Batch Adsorption Experiments

The effects of the operational parameters on the removal of CR dye, as summarised in Table 1, are illustrated in Figure 7.

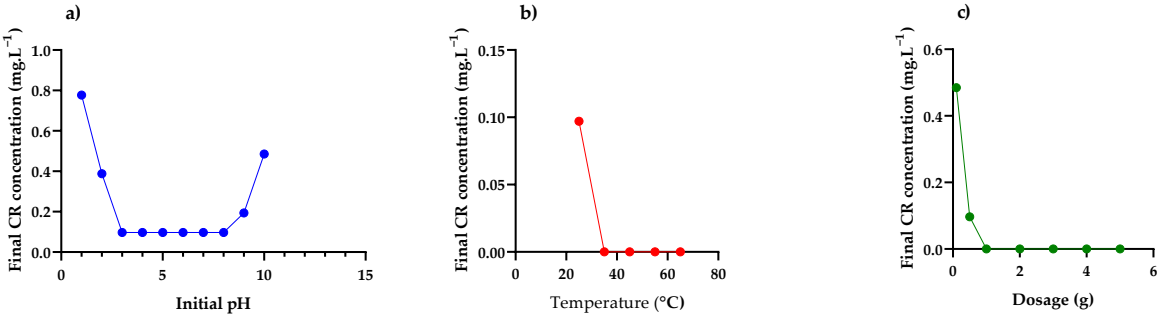

Figure 7. Effects of (**a**) Initial system pH, (**b**) Temperature, (**c**) Adsorbent dosage on the adsorption of CR dye.

Effect of Initial pH, Temperature and Adsorbent Dosage

As illustrated in Figure 7a, the highest percentage of removal was observed at a pH range of 3–8, after which the removal started to decrease. Mahapatra et al. [54] explained this behaviour as being a result of the interaction between hydroxide groups from the adsorbent and amine groups from CR dye.

As illustrated in Figure 7b, it was observed that the percentage removal increased with an increase in temperature and became constant after 35 °C. Therefore, 35 °C is an ideal temperature for the maximum removal of CR dye from an aqueous system.

As illustrated in Figure 7c, 1 g of the material was observed to remove 100% of CR dye. The complete removal of CR dye from an aqueous solution by PDFe/Al composite signifies the high efficiency of the material and enough availability of the adsorption sites.

3.3. Adsorption Kinetics

Adsorption kinetics for the adsorption of CR dye by PDFe/Al composite were studied to elucidate the varying mechanisms and rates of adsorption. The kinetic models are summarised in Table 3 with their graphical representations illustrated by Figure 8. The model parameters for the analytical form of the kinetic models in Table 3 were determined using the built-in iterative non-linear regression algorithm within the software package Graphpad Prism 9 (GraphPad Software Inc., San Diego, CA, USA).

Table 3. Kinetic models for the adsorption of CR dye by PDFe/Al composite.

Kinetic Law	Differential Form *	Analytical Form *	Fitted Parameters *	R^2/RMSE
Pseudo-first-order [55]	$\frac{dQ_t}{dt} = k_1(Q_e - Q_t)$	$Q_t = Q_e\left(1 - e^{-k_1 t}\right)$	k_1 = 1.85·min^{-1}	0.991/ 0.138 mg·g^{-1}
Pseudo-second-order [55]	$\frac{dQ_t}{dt} = k_1(Q_e - Q_t)^2$	$Q_t = \frac{\left(k_2 Q_e^2\right)t}{1+k_2 Q_e t}$	k_2 = 1.00 g·mg^{-1}·min^{-1}	0.998/ 0.0734 mg·g^{-1}
Two-phase adsorption [56–58]	$\frac{dQ_{t,slow}}{dt} = k_{slow}((1-\phi)Q_e - Q_{t,sloe})$ $\frac{dQ_{t,fast}}{dt} = k_{fast}\left(\phi Q_e - Q_{t,fast}\right)$ $\frac{dQ_t}{dt} = \frac{dQ_{t,slow}}{dt} + \frac{dQ_{t,fast}}{dt}$	$Q_t = Q_e\left((1-\phi)\left(1 - e^{-k_{fast}t}\right) + \phi\left(1 - e^{-k_{slow}t}\right)\right)$	k_{fast} = 3.18 min^{-1} k_{slow} = 0.128 min^{-1} ϕ = 0.863	1.000/ 0.0263 mg·g^{-1}
Crank internal mass transfer model [55]	$\frac{\partial Q_t}{\partial t} = \frac{D_e}{r^2}\frac{\partial}{\partial r}\left(\frac{r^2 \partial Q_t}{\partial r}\right)$	$\frac{Q_t}{Q_e} = \frac{6}{\pi^2}\sum_{n=1}^{\infty}\frac{1}{n^2}\exp\left(-\frac{D_e}{r^2}n^2\pi^2 t\right)$	D_e = 3.49 × 10^{-11} m^2·s^{-1}	0.991/0.0277 mg·g^{-1}
Weber and Morris [55,59]		$Q_t = k_{WM,i}t^{\frac{1}{2}} + C$, $k_{WM,i} = \frac{D_{e,i}}{r^2}$	D_{e1} = 3.49 × 10^{-11} m^2·s^{-1} D_{e2} = 4.19 × 10^{-14} m^2·s^{-1} D_{e3} = 0 m^2·s^{-1}	0.999/ 0.0421 mg·g^{-1}

* The definitions of the kinetic model parameters: General parameters: Q_t—amount of dye adsorbed per unit of adsorbent at time t (mg·g^{-1}); Q_e—equilibrium adsorption capacity of adsorbent (mg·g^{-1}); r = the average radius of the adsorbent particles (a conservative estimate of 16 µm was used as all particle diameters <32 µm). Pseudo-first-order (PFO) kinetics: k_1—the PFO rate constant (min^{-1}). Pseudo-second-order (PSO) kinetics: k_2—the PSO rate constant (g·mg^{-1}·min^{-1}). Two-phase adsorption (TPA) kinetics: k_{fast}—the rate constant for the fast TPA adsorption (min^{-1}); k_{slow}—the rate constant for the slow TPA adsorption (min^{-1}); ϕ—the fraction of adsorption taking place during the fast adsorption step (dimensionless). Crank internal mass transfer kinetic model: D_e—the effective diffusivity of the adsorbate in the system (m^2·s^{-1}). Weber and Morris kinetic model: $K_{WM,i}$—the Weber-Morris intra-particle diffusion rate constant for adsorption phase i (mg·g^{-1}); $D_{e,i}$—the effective diffusivity of the adsorbate during adsorption phase i (m^2·s^{-1}).

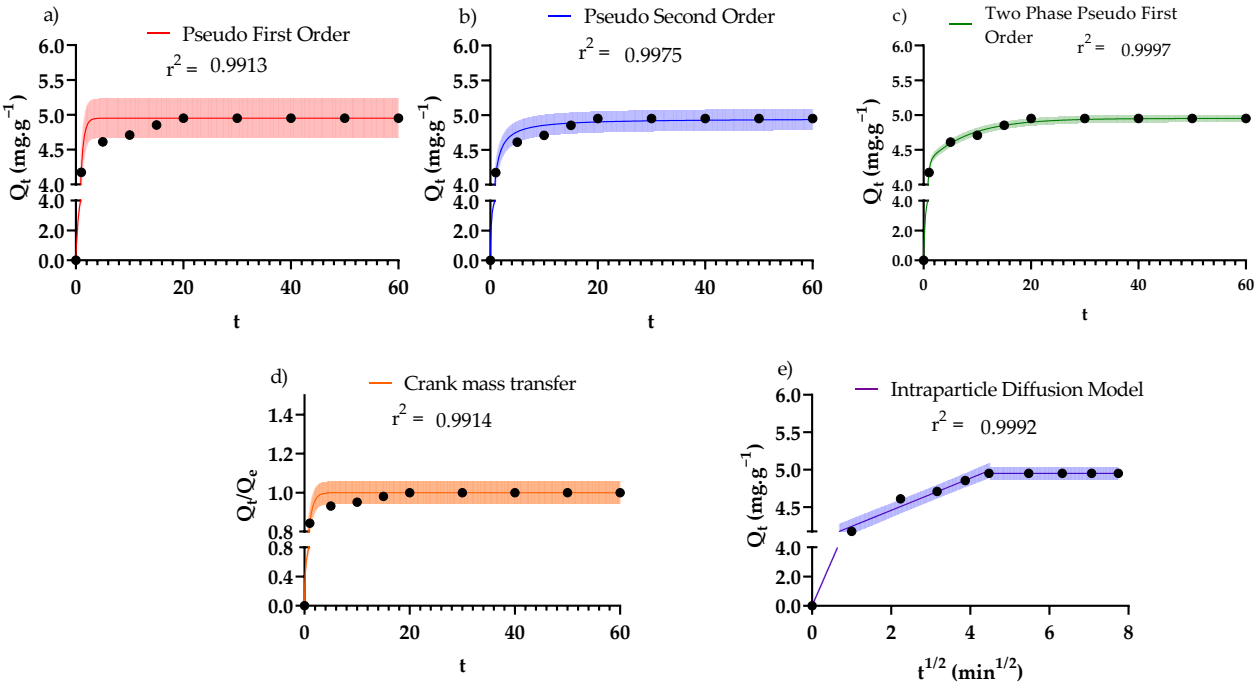

Figure 8. Different kinetic models fitted to the kinetic data for the adsorption of CR dye to the adsorbent. The models were: (**a**) pseudo-first-order, (**b**) pseudo-second-order, (**c**) two-phase pseudo-first-order, (**d**) Crank mass transfer model, and (**e**) intraparticle diffusion model. The shaded areas represent the 95% prediction intervals for the respective model fits. The optimised model parameters are reported in Table 3.

Figure 8a shows that good fits for the data were obtained from the pseudo-first-order (PFO) model (R^2 = 0.991); however, there is much uncertainty in the future observations relative to CR dye adsorption application, as seen in the very large 95% prediction interval due to the model's dependence on initial adsorbate concentrations, thus limiting the application of the PFO kinetic model. In Figure 8b, the pseudo-second-order (PSO) results were obtained in the same manner as PFO; however, the PSO suffers from the same limitations in terms of application as the PFO model, due to the dependence of the model on the initial adsorbate concentration.

In Figure 8c, the two-phase adsorption (TPA) model provides an improvement on the PFO and PSO kinetic models based on two parallel adsorption processes; namely, a rapid and a slow adsorption mechanism. The results obtained show a good fit (R^2 = 0.997) for the adsorption of CR dye. The TPA model provides insight into the mechanism of adsorption as well as the relative dominance of the adsorption kinetics on the adsorbent surface. Similar to what was proposed by Wang et al. [57], the current system involves compartmentalised adsorption with fast and slow adsorption taking place in parallel. In this system, the dominant adsorption takes place rapidly (86.3% of CR adsorbs during the fast phase) while relatively less adsorption follows slow adsorption kinetics (13.7% of CR adsorbs during the slow phase). This has significant implications for the scaling of the process, as it shows that more than 80% of the CR is removed within the first 2 min, followed by much slower adsorption. In addition, this kinetic model hints at multiple surface sites present on the surface with different adsorption characteristics [57]—this is explored further in the subsequent (Section 3.4). Figure 8d shows the Crank diffusion model, which was studied to determine the pore diffusion, based on the assumption that the adsorbent can be modelled as a porous sphere with constant effective diffusivity (D_e) [55]. The results obtained show a remarkably good fit for the CR adsorption data; a comparison of the fitted effective diffusivity ($D_e = 3.49 \times 10^{-11}$ $m^2 \cdot s^{-1}$) and the molecular diffusivity of CR (2.16×10^{-9} $m^2 \cdot s^{-1}$ [60]) showed that the system suffered from severe mass transfer

limitations. Figure 8e shows the Weber–Morris intraparticle diffusion model, which was investigated to study the effect of interparticle and intraparticle diffusion on the adsorption of CR dye. In this model, the first step of adsorption is intraparticle diffusion, the second phase is intraparticle, and the last phase is adsorption onto the adsorbent [61]. The data was fitted well (R^2 = 0.999), and the findings were good, where D_{e1} = 4.30 × 10^{-12} $m^2 \cdot s^{-1}$ and D_{e2} = 6.47 × 10^{-15} $m^2 \cdot s^{-1}$, supporting the observations from the Crank model (Figure 8d) of significant diffusion limitations in the system.

3.4. Adsorption Isotherms

Adsorption isotherms for the adsorption of CR dye by PDFe/Al were studied to elucidate the different mechanisms governing the adsorption process. The isotherm models are summarised in Table 4 with their graphical representations illustrated in Figure 9. The model parameters for the non-linear forms of the isotherm models in Table 4 were determined using Graphpad Prism 9 (GraphPad Software Inc., San Diego, CA, USA). The built-in non-linear regression algorithm involves an iterative process to minimise the error values between the measured data and predicted values.

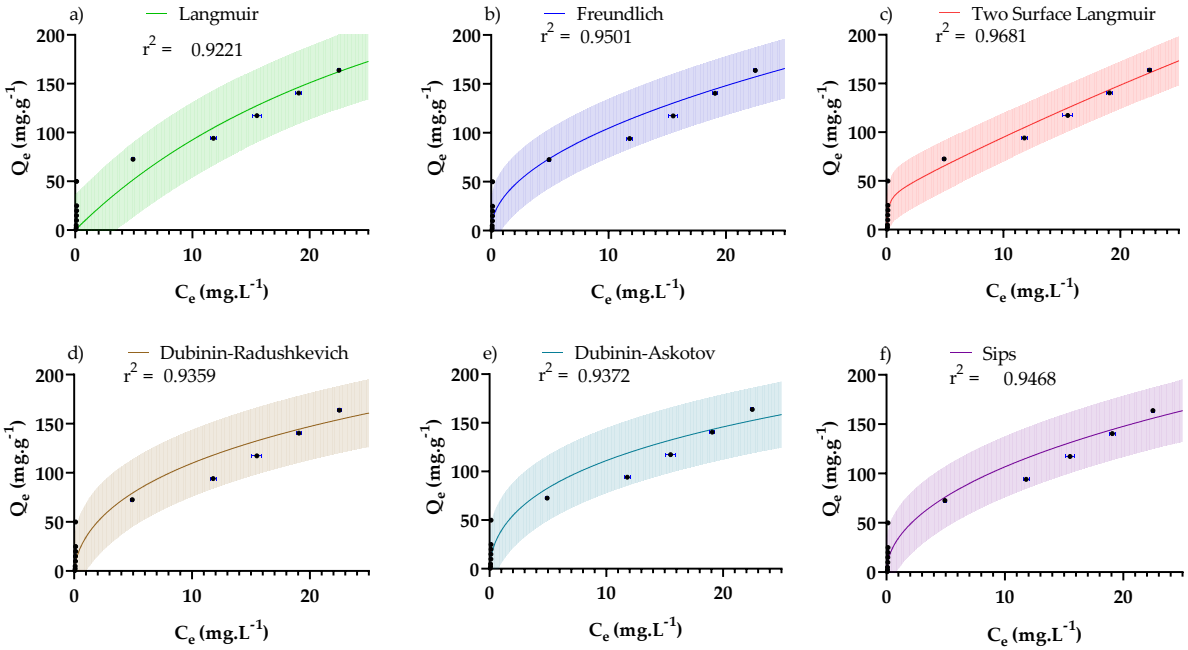

Figure 9. The non-linear fits of the isotherm models from (**a**) Langmuir, (**b**) Freundlich, (**c**) Two Surface Langmuir, (**d**) Dubinin–Radushkevich, (**e**) Dubinin–Askotov, and (**f**) Sips. The shaded areas indicate the 95% prediction intervals.

Table 4 provides a summary of the adsorption isotherms from the literature, where it can be observed that the models fitted the experimental data with a coefficient of determination R^2 < 0.99 and a root-mean-square error RMSE >12.7 $mg \cdot g^{-1}$, indicating that no single isotherm model was able to conclusively predict the equilibrium data. However, sufficiently good fits were obtained to provide some insights into the mechanisms responsible for adsorption.

Figure 9a shows the Langmuir adsorption isotherm where a maximum adsorption capacity of the material ($Q_{max,L}$) of 411 $mg \cdot g^{-1}$ was predicted. This is exceptionally high when compared to other reported studies. Of further interest is the value R_L = 0.775, indicating favourable adsorption conditions—0 < R_L < 1 is considered favourable for adsorption, R_L > 1 unfavourable for adsorption, R_L = 1 linear adsorption, and R_L = 0 irreversible adsorption [62]. This maximum adsorption capacity is not necessarily the true maximum adsorption of the adsorbent, as the Langmuir model only fits the data with a coefficient of determination of R^2 = 0.922.

Figure 9b shows the Freundlich adsorption isotherm, where the intensity parameter (n_F) gives an indication of the favourability of the adsorption—$n_F < 1$ is considered unfavourable, $n_F = 1$ designates linear adsorption, and $n_F > 1$ shows favourable adsorption [63,64]. In this system, n_F =1.99 indicates highly favourable adsorption.

Figure 9c shows the two-surface Langmuir adsorption isotherm, which assumes that the surface of the adsorbent has multiple surface types with different adsorption properties.

Table 4. Isotherms and accompanying fitting parameters used to model the CR isotherm data.

Isotherm	Non-Linear Form *	Fitted Parameters *	R^2/RMSE
Langmuir [55,65,66]	$Q_e = \frac{k_L Q_{max,L} C_e}{1+k_L C_e}$,	$k_L = 0.0290$ L·mg^{-1} $Q_{max} = 411$ mg·g^{-1} $R_L = 0.775$	0.922/ 17.7 mg·g^{-1}
Freundlich [66]	$Q_e = K_F C_e^{\frac{1}{n}}$	$K_F = 32.9$ mg·g^{-1}(L·mg^{-1})$^{\frac{1}{n_F}}$ $n_F = 1.99$	0.950/ 14.2 mg·g^{-1}
Two-surface Langmuir [65]	$Q_e = \sum_{i=1}^{2} \frac{k_{L,i}(T) Q_{max,i} C_e}{1+k_{L,i}(T) C_e}$,	$Q_{max,1} = 33.0$ mg·g^{-1}, $k_{L,1} = 6.802$ L·mg^{-1} $Q_{max,2} = 1270$ mg·g^{-1} $k_{L,2} = 0.004818$ L·mg^{-1}, $R_{L,1} = 0.0145$ $R_{L,2} = 0.95$	0.968 11.34 mg·g^{-1}
Dubinin–Radushkevich [66]	$Q_e = Q_{max,DR} \exp\left\{-\left[\frac{RTln(C_S/C_e)}{E_{DR}}\right]^2\right\}$	$E_{DR} = 15.0$ kJ·mol^{-1} $Q_{max,DR} = 658$ mg·g^{-1}	0.936/ 16.1 mg·g^{-1}
Dubinin–Astokov [66]	$Q_e = Q_{max,DA} \exp\left\{-\left[\frac{RTln(C_S/C_e)}{E_{DA}}\right]^{n_{DA}}\right\}$	$E_{DA} = 14.7$ kJ·.mol^{-1} $Q_{max,DA} = 658$ mg·g^{-1} $n_{DA} = 1.85$	0.937/ 15.9 mg·g^{-1}
Sips [67]	$Q_e = \frac{K_S Q_{max,S} C_e^{\frac{1}{n_S}}}{1+K_S C_e^{\frac{1}{n_S}}}$	$Q_{max,S} = 1350$ mg·g^{-1} $K_S = 0.0261$ g·g^{-1}(L·mg^{-1})$^{\frac{1}{n_S}}$ $n_S = 1.93$	0.947/14.6 mg·g^{-1}

* The definitions of the isotherm parameters: Langmuir isotherm: k_L—the Langmuir equilibrium constant (L·mg^{-1}); $Q_{max,L}$—the Langmuir maximum adsorption capacity (mg·g^{-1}); R_L—the Langmuir separation factor (dimensionless). Freundlich isotherm: K_F—the Freundlich intensity parameter ((mg·g^{-1})(L·mg^{-1})$^{1/nF}$); n_F—Freundlich isotherm exponent (dimensionless). Two-surface Langmuir isotherm: $k_{L,i}$—the Langmuir equilibrium constant for surface i (L·mg^{-1}); $Q_{max,i}$—the Langmuir maximum adsorption capacity for surface i (mg·g^{-1}); $R_{L,i}$—the Langmuir separation factor for surface i (dimensionless). Sips isotherm: K_S—the Sips constant ((mg·g^{-1})(L·mg^{-1})$^{1/nS}$); $Q_{max,S}$—the Sips maximum adsorption capacity (mg·g^{-1}); n_F—Sips isotherm exponent (dimensionless). Dubinin–Radushkevich (DR) isotherm: $Q_{max,DR}$—the DR maximum adsorption capacity (mg·g^{-1}); R—the ideal gas constant (8.314 J·mol^{-1}·K^{-1}); T—temperature in the system (K); C_S—saturation concentration of the adsorbate (33 g·L^{-1} [68]); E_{DR}—energy required to adsorb an adsorbate from infinity to the adsorbent surface (kJ·mol^{-1}). Dubinin–Astokov (DA) isotherm: $Q_{max,DA}$—the DA maximum adsorption capacity (mg·g^{-1}); T—temperature in the system (K); C_S—saturation concentration of the adsorbate (33 g·L^{-1} [68]); E_{DA}—energy required to adsorb an adsorbate from infinity to the adsorbent surface (kJ·mol^{-1}); n_{DA}—DA isotherm exponent (dimensionless).

The results from this model were markedly better than that for the single surface Langmuir model with $Q_{max,1}$ = 33.0 mg·g^{-1} and $Q_{max,2}$ = 1270 mg·g^{-1} for two surfaces, giving a total maximum adsorption of 1303 mg·g^{-1}—significantly greater than that previously reported for CR adsorption. However, since the total maximum adsorption capacity is a gross extrapolation of the experimental data, the more conservative Langmuir adsorption capacity ($Q_{max,L}$) was adopted as the official maximum adsorption capacity for the study. What is of most interest is that the two-surface Langmuir model proposes that the adsorbent surface consists of two separate adsorption surfaces with different energies and sorption properties on which parallel adsorption takes place [65] (likely related to TPA kinetics—Table 3). The first surface exhibited irreversible adsorption with $Q_{max,1}$ = 33.0 mg·g^{-1}, while the second adsorption surface exhibited reversible adsorption with a remarkably large $Q_{max,2}$ = 1270 mg·g^{-1}. This is supported by the observations that the $R_{L,1}$ = 0.0145 indicates nearly irreversible adsorption, while $R_{L,2}$ = 0.95 indicates highly favourable adsorption conditions [62].

Figure 9d shows the Dubinin–Radushkevich (DR) isotherm, which predicts dilute liquid adsorption behaviour [69]. This isotherm was subsequently generalised to the Dubinin–Astokov (DA) isotherm (Figure 9e), which accounts for non-ideal adsorption behaviour [70].

Results from the DR and DA non-linear fits (Table 4) illustrate comparable adsorption capacities to Langmuir and two-surface Langmuir models ($Q_{max,DR}$ = 658 mg·g^{-1} and $Q_{max,DA}$ = 658 mg·g^{-1}). The adsorption energies for D_R and D_A isotherms were determined and found to be E_{DR} = 15.0 kJ·mol^{-1} and E_{DA} = 14.7 kJ·mol^{-1}. The values for the adsorption energies indicate a diffusion-controlled adsorption mechanism—energies >16 kJ·mol^{-1} designate chemisorption, energies <8 kJ·mol^{-1} correspond to physisorption, and energies between 8 and 16 kJ·mol^{-1} indicate mass transfer limited diffusion [71]

Figure 9f shows the Sips adsorption isotherm, where $Q_{max,S}$ = 1350 mg·g^{-1}, K_S = 204.15 and n_S = 1.93 for the Sips isotherm. According to Keren et al. [72], the Sips adsorption isotherm is a flexible isotherm model which corresponds to different isotherm models depending on the value for n_S. The Sips isotherm reduces to the Langmuir isotherm for n_S = 1, while a value for n_S > 1 results in a sorbate–sorption site interaction characterised by a Gaussian distribution (known as the Langmuir–Freundlich model). A value for n_S < 1 indicates a cooperative reaction between sorption sites and n sorbate molecules; this type of adsorption is characterised by sigmoidal adsorption isotherm data. The Sips isotherm model further reduces to the Freundlich model for n_S > 1 and at low adsorbate concentrations (when $K_S C^{1/ns} \ll 1$). The implication for the current study is that the system corresponds to the Langmuir–Freundlich model which shows a distributive adsorbate–sorption site interaction that deviates significantly from the Langmuir isotherm model but corresponds well with the Freundlich model at low adsorbate loadings. The value for n_S = 1.93 shows that favourable adsorption conditions are present (similar to the Freundlich isotherm). The Sips isotherm model links strongly to the two-surface Langmuir model which predicts a heterogeneous surface with two main surface sites showing differing adsorption characteristics.

The values for the Q_{max} for both the two-surface Langmuir and Sips models are >1300 mg·g^{-1}, which is remarkably high for CR adsorption. However, as indicated before due to the uncertainty inherent in such significant extrapolation, the $Q_{max,L}$ was adopted as the official maximum adsorption capacity of the study.

3.5. Comparison of PDFe/Al with Other Adsorbents

Table 5 summarises prominent CR adsorption studies using Al- and Fe-based adsorbents from the literature, thereby providing a comparison of the results for the current study. From Table 5, it can be seen that the current study compares well with other Fe- and Al-based adsorbents for CR adsorption in terms of adsorption capacity ($Q_{max,L}$) and the favourability of adsorption (n_F > 1). This is especially pertinent considering that the only materials to outcompete the current materials in terms of $Q_{max,L}$ were synthesised using laboratory-grade chemicals, whereas the PDFe/Al was synthesised using *bona fide* AMD. In addition, the materials showing higher adsorption favourability (higher n_F) displayed significantly lower maximum adsorption capacities, indicating that PDFe/Al represented a highly desirable combination of high adsorption capacity and favourability towards CR adsorption.

Table 5. Comparison of PDFe/Al with other Al- and Fe-based adsorbents for CR adsorption in order of decreasing $Q_{max,L}$ values.

Adsorbent	$Q_{max,L}$ *	n_F **	Reference
BTCS functionalised Fe_3O_4 nanoparticles	630 $mg \cdot g^{-1}$	1.9596	[73]
γ-Fe_2O_3–γ-Al_2O_3	416.7 $mg \cdot g^{-1}$	1.13	[54]
PDFe/Al	411 $mg \cdot g^{-1}$	1.99	This study
Iron doped PVA-chitosan	315 $mg \cdot g^{-1}$	6.34	[74]
$Fe_xCo_{3-x}O_4$	160.3 $mg \cdot g^{-1}$	1.44	[75]
Calcium Alginate Beads—nano-goethite	181.1 ± 2.32 $mg \cdot g^{-1}$	2.431 ± 0.343	[76]
Fe_2O_3–Al_2O_3	126.58 $mg \cdot g^{-1}$	1.85	[54]
Graphine Oxide-$CuFe_2O_4$	114.21 $mg \cdot g^{-1}$	1.223	[77]
Alumina-Zirconia	41.07 $mg \cdot g^{-1}$	2.177	[78]
Nano bio-clay composite (Kaolinite/Ulva Lactuca)	23.7529 $mg \cdot g^{-1}$	1.68	[79]
α-Fe_2O_3–α-Al_2O_3	1.422 $mg \cdot g^{-1}$	−0.665	[54]

* $Q_{max,L}$—the Langmuir maximum adsorption capacity ($mg \cdot g^{-1}$); ** n_F—the Freundlich isotherm exponent (dimensionless).

3.6. Regeneration Study

As illustrated in Figure 10, a regeneration study was performed to regenerate the material after CR dye adsorption.

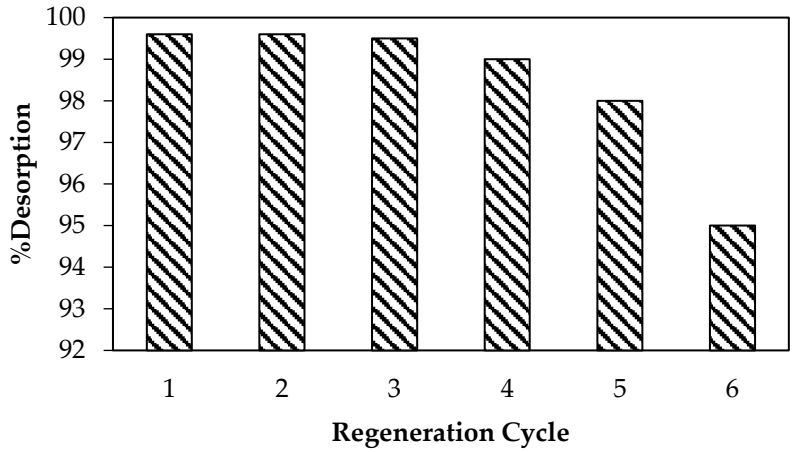

Figure 10. Recovery efficiency of PDFe/Al after CR dye adsorption.

The material showed the potential to be reused more than four times for CR dye adsorption. It should be noted that even during the sixth regeneration cycle the % desorption ≈ 95%, indicating a significantly stable and regenerable adsorbent for industrial application.

3.7. Adsorption Mechanism

The proposed adsorption mechanism for CR adsorption is summarised in Figure 11.

The adsorption of CR dye by PDFe/Al appears to be predominantly diffusion-controlled, with the greatest predicted effective diffusivity of 3.49×10^{-11} $m^2 \cdot s^{-1}$ being two orders of magnitude smaller than the molecular diffusivity of CR of 2.16×10^{-9} $m^2 \cdot s^{-1}$ [60]. This is further supported by the predicted Dubinin–Radushkevich and Dubinin–Astokov energies of adsorption of E_{DR} = 15.0 $kJ \cdot mol^{-1}$ and E_{DA} = 14.7 $kJ \cdot mol^{-1}$, both indicating a diffusion-controlled adsorption mechanism [71]. The diffusion-controlled system is likely a reason for the difficulty in conclusively determining if physisorption or chemisorption is dominant in the system (relatively poor fits for both PFO and PSO kinetics models). The two-surface Langmuir model indicated that the adsorbent consisted of two distinct adsorption surfaces, one irreversible with an adsorption capacity of 33 $mg \cdot g^{-1}$ and one reversible with and adsorption capacity of 1270 $mg \cdot g^{-1}$. This multi-surface characteristic is supported by two-phase adsorption kinetics, showing a fast and slow adsorption process taking place in parallel. Finally, it was observed that the adsorption of CR on the

adsorbent surface induced significant internal strain within the adsorbent, which resulted in deformation, cracking, and subsequent increased adsorption area and volume within the adsorbent. This increased area, coupled with electrostatic interactions and additional covalent/donor–acceptor interactions between the surface of the adsorbent and CR dye ions, could explain the high adsorption of CR dye ions by PDFe/Al [80].

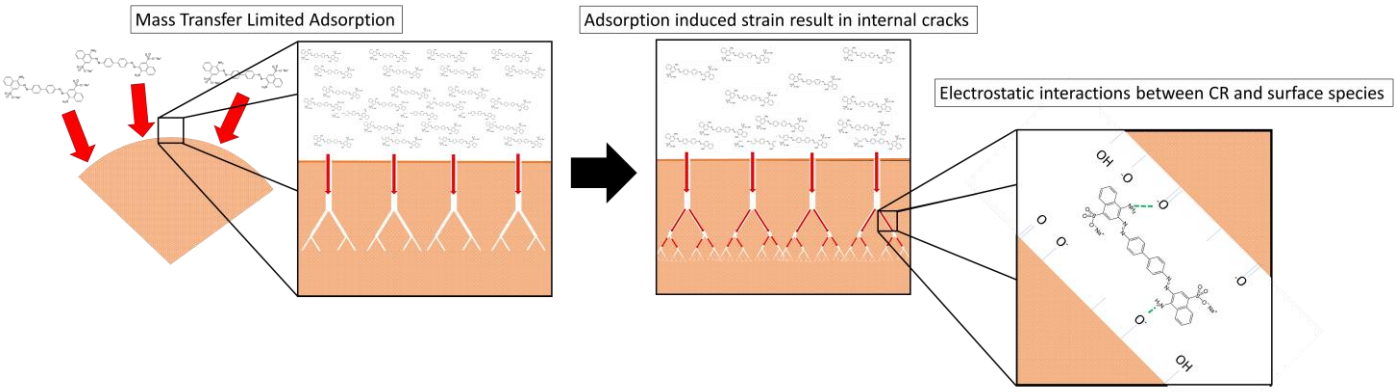

Figure 11. Proposed adsorption mechanism.

4. Practical Implications of This Study

This study has demonstrated multiple technical feasibilities in the use of the synthesised nanocomposite for the removal of CR dye. Henceforth, upscaling this technology to a viable industrial scale could be possible, specifically considering the amount of mine water being generated in South Africa. Furthermore, findings from our laboratory assays have confirmed the efficacy of the synthesised PDFe/Al; the next stage should be to pilot the application for the removal of CR using real industrial effluents.

Future work and Recommendations:

- Column tests will be carried out to assess the developed materials' ability to remove CR continuously.
- A techno-economic analysis of the suggested material should be performed to determine the technology's economic viability.
- The doping of the material should be considered to boost its adsorption capacity, hence increasing the proposed materials' adsorption efficiency.
- A life-cycle analysis of the proposed system will be used to determine the environmental sustainability of the technology.

5. Conclusions

This double-edged study presents the first known investigation into the adsorption of CR by PDFe/Al synthesised from *bona fide* AMD. The study successfully demonstrated the highly effective removal of CR from aqueous solution by PDFe/Al. The optimised conditions for CR dye adsorption were found to be: 100 $mg{\cdot}L^{-1}$ initial CR dye concentration, 1 g of PDFe/Al in 500 mL adsorbate solution, pH 3–8, 20 min agitation, and a temperature of 35 °C. The synthesised PDFe/Al had a Langmuir adsorption capacity of 411 $mg{\cdot}g^{-1}$ CR dye with >99% removal of CR—one of the highest for CR adsorption. The adsorption mechanism was found to be significantly diffusion-limited, with a dual-site adsorption surface responsible for adsorption. It was further found that CR adsorption induced strain and deformation within the PDFe/Al, resulting in internal crack formation and a consequent increase in pore surface area (37.58 $m^2.g^{-1}$ before adsorption vs 134.46 $m^2.g^{-1}$ after adsorption) and pore volume (0.0621 $cm^3.\ g^{-1}$ before adsorption vs 0.1137 $cm^3.\ g^{-1}$ after adsorption). This remarkable increase in the surface area could provide an explanation of the notable adsorption capacity measured. Finally, it was determined that the PDFe/Al could be regenerated and reused more than four times with minimal loss in adsorption

efficiency. The current study successfully valorised and beneficiated AMD and provides an avenue to foster and grow the circular economy in wastewater treatment.

Author Contributions: Conceptualisation, K.L.M., V.M. and J.P.M.; methodology, K.L.M.; software, H.G.B.; validation, V.M., N.H. and H.G.B.; formal analysis, K.L.M. and H.G.B.; investigation, K.L.M.; resources, V.M., J.P.M., N.H. and H.G.B.; data curation, K.L.M., H.G.B. and V.M.; writing—original draft preparation, K.L.M., V.M. and H.G.B.; writing—review and editing, K.L.M., V.M., N.H. and H.G.B.; visualisation, K.L.M. and H.G.B.; supervision, H.G.B., V.M. and J.P.M.; project administration, H.G.B.; funding acquisition, N.H. and H.G.B. All authors have read and agreed to the published version of the manuscript.

Funding: This research was funded by the National Research Foundation (NRF) of South Africa: Grant number SFH160713177910, the Max-Buchner-Forschungsstiftung of DECHEMA e.V.: Grant number 3824, Austrian Agency for International Cooperation in Education and Research (OeAD): Africa UniNet P056, APPEAR Prep222, BG 01/2021, KOEF 01/2019 and TW 01/2021.

Institutional Review Board Statement: Not applicable.

Informed Consent Statement: Not applicable.

Data Availability Statement: The data presented in this study are openly available in the University of Pretoria Research Data Repository at doi:10.25403/UPresearchdata.19228875.

Conflicts of Interest: The authors declare no conflict of interest.

References

1. Zhou, Y.; Lu, J.; Zhou, Y.; Liu, Y. Recent advances for dyes removal using novel adsorbents: A review. *Environ. Pollut.* **2019**, *252*, 352–365. [CrossRef] [PubMed]
2. Masindi, V.; Foteinis, S.; Chatzisymeon, E. Co-treatment of acid mine drainage and municipal wastewater effluents: Emphasis on the fate and partitioning of chemical contaminants. *J. Hazard. Mater.* **2022**, *421*, 126677. [CrossRef] [PubMed]
3. Jooste, S.; Thirion, C. An ecological risk assessment for a South African acid mine drainage. *Water Sci. Technol.* **1999**, *39*, 297–303. [CrossRef]
4. Waters, A.S.; Webster-Brown, J.G. Assessing aluminium toxicity in streams affected by acid mine drainage. *Water Sci. Technol.* **2013**, *67*, 1764–1772. [CrossRef] [PubMed]
5. Pavithra, K.G.; Kumar, S.P.; Jaikumar, V.; Rajan, P.S. Removal of colorants from wastewater: A review on sources and treatment strategies. *J. Ind. Eng. Chem.* **2019**, *75*, 1–19. [CrossRef]
6. Ohemeng-Boahen, G.; Sewu, D.D.; Tran, H.N.; Woo, S.H. Enhanced adsorption of congo red from aqueous solution using chitosan/hematite nanocomposite hydrogel capsule fabricated via anionic surfactant gelation. *Colloids Surf. A Physicochem. Eng. Asp.* **2021**, *625*, 126911. [CrossRef]
7. Masindi, V.; Osman, M.S.; Mbhele, R.N.; Rikhotso, R. Fate of pollutants post treatment of acid mine drainage with basic oxygen furnace slag: Validation of experimental results with a geochemical model. *J. Clean. Prod.* **2018**, *172*, 2899–2909. [CrossRef]
8. Rezaie, B.; Anderson, A. Sustainable resolutions for environmental threat of the acid mine drainage. *Sci. Total Environ.* **2020**, *717*, 137211. [CrossRef]
9. Zhu, G.; Wu, X.; Ge, J.; Liu, F.; Zhao, W.; Wu, C. Influence of mining activities on groundwater hydrochemistry and heavy metal migration using a self-organizing map (SOM). *J. Clean. Prod.* **2020**, *257*, 120664. [CrossRef]
10. Bologo, V.; Maree, J.P.; Carlsson, F. Application of magnesium hydroxide and barium hydroxide for the removal of metals and sulphate from mine water. *Water SA* **2012**, *38*, 23–28. [CrossRef]
11. Park, I.; Tabelin, C.B.; Jeon, S.; Li, X.; Seno, K.; Ito, M.; Hiroyoshi, N. A review of recent strategies for acid mine drainage prevention and mine tailings recycling. *Chemosphere* **2019**, *219*, 588–606. [CrossRef] [PubMed]
12. Acharya, B.S.; Kharel, G. Acid mine drainage from coal mining in the United States–An overview. *J. Hydrol.* **2020**, *588*, 125061. [CrossRef]
13. Cook, A.; Finkelman, R.B.; Fourie, A. Mineral and Fuel Extraction: Health Consequences. In *Encyclopedia of Environmental Health*, 2nd ed.; Nriagu, J., Ed.; Elsevier: Oxford, UK, 2019; pp. 408–414. ISBN 978-0-444-63952-3. [CrossRef]
14. Holmes, S. Department of Water Affairs and Forestry. In *South African Water Quality Guidelines, Field Guide*, 1st ed.; Department of Water Affairs and Forestry: Pretoria, South Africa, 1996; Volume 8.
15. U.S. Environmental Protection Agency (EPA). *Water Quality Standards Handbook: Chapter 3: Water Quality Criteria*; EPA Office of Water, Office of Science and Technology: Washington, DC, USA, 2017.
16. Akinwekomi, V.; Maree, J.P.; Zvinowanda, C.; Masindi, V. Synthesis of magnetite from iron-rich mine water using sodium carbonate. *J. Environ. Chem. Eng.* **2017**, *5*, 2699–2707. [CrossRef]

17. Akinwekomi, V.; Maree, J.P.; Masindi, V.; Zvinowanda, C.; Osman, M.S.; Foteinis, S.; Mpenyana-Monyatsi, L.; Chatzisymeon, E. Beneficiation of acid mine drainage (AMD): A viable option for the synthesis of goethite, hematite, magnetite, and gypsum–Gearing towards a circular economy concept. *Miner. Eng.* **2020**, *148*, 106204. [CrossRef]
18. Naidu, G.; Ryu, S.; Thiruvenkatachari, R.; Choi, Y.; Jeong, S.; Vigneswaran, S. A critical review on remediation, reuse, and resource recovery from acid mine drainage. *Environ. Pollut.* **2019**, *247*, 1110–1124. [CrossRef]
19. Nleya, Y.; Simate, G.S.; Ndlovu, S. Sustainability assessment of the recovery and utilisation of acid from acid mine drainage. *J. Clean. Prod.* **2016**, *113*, 17–27. [CrossRef]
20. Wei, X.; Viadero, R.C., Jr.; Bhojappa, S. Phosphorus removal by acid mine drainage sludge from secondary effluents of municipal wastewater treatment plants. *Water Res.* **2008**, *42*, 3275–3284. [CrossRef]
21. Kefeni, K.K.; Msagati, T.A.M.; Nkambule, T.T.I.; Mamba, B.B. Synthesis and application of hematite nanoparticles for acid mine drainage treatment. *J. Environ. Chem. Eng.* **2018**, *6*, 1865–1874. [CrossRef]
22. Muedi, K.L.; Brink, H.G.; Masindi, V.; Maree, J.P. Effective removal of arsenate from wastewater using aluminium enriched ferric oxide-hydroxide recovered from authentic acid mine drainage. *J. Hazard. Mater.* **2021**, *414*, 125491. [CrossRef]
23. Wei, X.; Viadero, R.C. Adsorption and Precoat Filtration Studies of Synthetic Dye Removal by Acid Mine Drainage Sludge. *J. Environ. Eng.* **2007**, *133*, 633–640. [CrossRef]
24. Ngulube, T.; Gumbo, J.R.; Masindi, V.; Maity, A. An update on synthetic dyes adsorption onto clay based minerals: A state-of-art review. *J. Environ. Manag.* **2017**, *191*, 35–57. [CrossRef] [PubMed]
25. Chattopadhyay, D.P. Chemistry of dyeing. In *Handbook of Textile and Industrial Dyeing*; Clark, M., Ed.; Woodhead Publishing Limited: Sawston, UK, 2011; pp. 150–183. [CrossRef]
26. Mu, B.; Wang, A. Adsorption of dyes onto palygorskite and its composites: A review. *J. Environ. Chem. Eng.* **2016**, *4*, 1274–1294. [CrossRef]
27. Hu, M.; Yan, X.; Hu, X.; Zhang, J.; Feng, R.; Zhou, M. Ultra-high adsorption capacity of MgO/SiO_2 composites with rough surfaces for Congo red removal from water. *J. Colloid Interface Sci.* **2018**, *510*, 111–117. [CrossRef] [PubMed]
28. Zhang, J.; Yan, X.; Hu, M.; Hu, X.; Zhou, M. Adsorption of Congo red from aqueous solution using ZnO-modified SiO_2 nanospheres with rough surfaces. *J. Mol. Liq.* **2018**, *249*, 772–778. [CrossRef]
29. Toor, M.; Jin, B. Adsorption characteristics, isotherm, kinetics, and diffusion of modified natural bentonite for removing diazo dye. *Chem. Eng. J.* **2012**, *187*, 79–88. [CrossRef]
30. Toor, M.; Jin, B.; Dai, S.; Vimonses, V. Activating natural bentonite as a cost-effective adsorbent for removal of Congo-red in wastewater. *J. Ind. Eng. Chem.* **2015**, *21*, 653–661. [CrossRef]
31. Sasmal, D.; Maity, J.; Kolya, H.; Tripathy, T. Study of congo red dye removal from its aqueous solution using sulfated acrylamide and N, N-dimethyl acrylamide grafted amylopectin. *J. Water Process Eng.* **2017**, *18*, 7–19. [CrossRef]
32. Miandad, R.; Kumar, R.; Barakat, M.A.; Basheer, C.; Aburiazaiza, A.S.; Nizami, A.S.; Rehan, M. Untapped conversion of plastic waste char into carbon-metal LDOs for the adsorption of Congo red. *J. Colloid Interface Sci.* **2018**, *511*, 402–410. [CrossRef]
33. Ausavasukhi, A.; Kampoosaen, C.; Kengnok, O. Adsorption characteristics of Congo red on carbonized leonardite. *J. Clean. Prod.* **2016**, *134*, 506–514. [CrossRef]
34. Abdel-Khalek, M.A.; Abdel Rahman, M.K.; Francis, A.A. Exploring the adsorption behavior of cationic and anionic dyes on industrial waste shells of egg. *J. Environ. Chem. Eng.* **2017**, *5*, 319–327. [CrossRef]
35. Dhal, J.P.; Sethi, M.; Mishra, B.G.; Hota, G. MgO nanomaterials with different morphologies and their sorption capacity for removal of toxic dyes. *Mater. Lett.* **2015**, *141*, 267–271. [CrossRef]
36. Hou, R.; Gao, Y.; Zhu, H.; Yang, G.; Liu, W.; Huo, Y.; Xie, Z.; Li, H. Coupling system of Ag/BiOBr photocatalysis and direct contact membrane distillation for complete purification of N-containing dye wastewater. *Chem. Eng. J.* **2017**, *317*, 386–393. [CrossRef]
37. Zhao, S.; Wang, Z. A loose nano-filtration membrane prepared by coating HPAN UF membrane with modified PEI for dye reuse and desalination. *J. Membr. Sci.* **2017**, *524*, 214–224. [CrossRef]
38. Dotto, G.L.; Lima, E.C.; Pinto, L.A.A. Biosorption of food dyes onto Spirulina platensis nanoparticles: Equilibrium isotherm and thermodynamic analysis. *Bioresour. Technol.* **2012**, *103*, 123–130. [CrossRef] [PubMed]
39. Mohy Eldin, M.S.; Aly, K.M.; Khan, Z.A.; Meky, A.E.; Saleh, T.S.; Elbogamy, A.S. Development of novel acid–base ions exchanger for basic dye removal: Phosphoric acid doped pyrazole-g-polyglycidyl methacrylate. *Desalin. Water Treat.* **2016**, *57*, 24047–24055. [CrossRef]
40. Gao, B.-Y.; Yue, Q.-Y.; Wang, Y.; Zhou, W.-Z. Color removal from dye-containing wastewater by magnesium chloride. *J. Environ. Manag.* **2007**, *82*, 167–172. [CrossRef]
41. Ziane, S.; Bessaha, F.; Marouf-Khelifa, K.; Khelifa, A. Single and binary adsorption of reactive black 5 and Congo red on modified dolomite: Performance and mechanism. *J. Mol. Liq.* **2018**, *249*, 1245–1253. [CrossRef]
42. Tan, K.B.; Vakili, M.; Horri, B.A.; Poh, P.E.; Abdullah, A.Z.; Salamatinia, B. Adsorption of dyes by nanomaterials: Recent developments and adsorption mechanisms. *Sep. Purif. Technol.* **2015**, *150*, 229–242. [CrossRef]
43. Sriram, G.; Uthappa, U.T.; Losic, D.; Kigga, M.; Jung, H.-Y.; Kurkuri, M.D. Mg–Al-Layered Double Hydroxide (LDH) Modified Diatoms for Highly Efficient Removal of Congo Red from Aqueous Solution. *Appl. Sci.* **2020**, *10*, 2285. [CrossRef]
44. Dhal, J.; Mishra, B.; Hota, G. Ferrous oxalate, maghemite and hematite nanorods as efficient adsorbents for decontamination of Congo red dye from aqueous system. *Int. J. Environ. Sci. Technol.* **2014**, *12*, 1845–1856. [CrossRef]

45. Bordoloi, S.; Nath, S.K.; Gogoi, S.; Dutta, R.K. Arsenic and iron removal from groundwater by oxidation-coagulation at optimized pH: Laboratory and field studies. *J. Hazard. Mater.* **2013**, *260*, 618–626. [CrossRef] [PubMed]
46. Wang, X.; Cheng, B.; Zhang, L.; Yu, J.; Li, Y. Synthesis of MgNiCo LDH hollow structure derived from ZIF-67 as superb adsorbent for Congo red. *J. Colloid Interface Sci.* **2022**, *612*, 598–607. [CrossRef]
47. Mei, L.; Liao, L.; Wang, Z.; Xu, C. Interactions between Phosphoric/Tannic Acid and Different Forms of FeOOH. *Adv. Mater. Sci. Eng.* **2015**, *2015*, 250836. [CrossRef]
48. Mikhaylov, V.I.; Martakov, I.S.; Gerasimov, E.Y.; Sitnikov, P.A. Study of heteroaggregation and properties of sol-gel AlOOH-Fe_3O_4 composites. *Heliyon* **2020**, *6*, 12. [CrossRef] [PubMed]
49. Dolino, G.; Bellet, D.; Faivre, C. Adsorption strains in porous silicon. *Phys. Rev. B-Condens. Matter Mater. Phys.* **1996**, *54*, 17919–17929. [CrossRef]
50. Gor, G.Y.; Huber, P.; Bernstein, N. Adsorption-induced deformation of nanoporous materials-A review. *Appl. Phys. Rev.* **2017**, *4*, 011303. [CrossRef]
51. Gor, G.Y.; Bernstein, N. Revisiting Bangham's law of adsorption-induced deformation: Changes of surface energy and surface stress. *Phys. Chem. Chem. Phys.* **2016**, *18*, 9788–9798. [CrossRef]
52. Sing, K.S.W. Reporting physisorption data for gas/solid systems with special reference to the determination of surface area and porosity (Recommendations 1984). *Pure Appl. Chem.* **1985**, *57*, 603–619. [CrossRef]
53. Li, X.D.; Fang, Y.M.; Wu, S.Q.; Zhu, Z.Z. Adsorption of alkali, alkaline-earth, simple and 3d transition metal, and nonmetal atoms on monolayer MoS_2. *AIP Adv.* **2015**, *5*, 57143. [CrossRef]
54. Mahapatra, A.; Mishra, B.G.; Hota, G. Adsorptive removal of Congo red dye from wastewater by mixed iron oxide-alumina nanocomposites. *Ceram. Int.* **2013**, *39*, 5443–5451. [CrossRef]
55. Largitte, L.; Pasquier, R. A review of the kinetics adsorption models and their application to the adsorption of lead by an activated carbon. *Chem. Eng. Res. Des.* **2016**, *109*, 495–504. [CrossRef]
56. Brusseau, M.L.; Jessup, R.E.; Suresh, P.; Rao, C. Nonequilibrium Sorption of Organic Chemicals: Elucidation of Rate-Limiting Processes. *Environ. Sci. Technol.* **1991**, *25*, 134–142. [CrossRef]
57. Wang, Z.; Zhao, J.; Song, L.; Mashayekhi, H.; Chefetz, B.; Xing, B. Adsorption and desorption of phenanthrene on carbon nanotubes in simulated gastrointestinal fluids. *Environ. Sci. Technol.* **2011**, *45*, 6018–6024. [CrossRef] [PubMed]
58. Cornelissen, G.; Van Noort, P.C.M.; Parsons, J.R.; Govers, H.A.J. Temperature dependence of slow adsorption and desorption kinetics of organic compounds in sediments. *Environ. Sci. Technol.* **1997**, *31*, 454–460. [CrossRef]
59. Weber, W.J.; Morris, J.C. Kinetics of Adsorption on Carbon from Solution. *J. Sanit. Eng. Div.* **1963**, *89*, 31–60. [CrossRef]
60. Nakagaki, M. The Diffusion of Dye Solutions. *Bull. Chem. Soc. Jpn.* **1950**, *23*, 104–107. [CrossRef]
61. Bhaumik, M.; Maity, A.; Brink, H.G. Zero valent nickel nanoparticles decorated polyaniline nanotubes for the efficient removal of Pb(II) from aqueous solution: Synthesis, characterization and mechanism investigation. *Chem. Eng. J.* **2021**, *417*, 127910. [CrossRef]
62. Vimonses, V.; Lei, S.; Jin, B.; Chow, C.W.K.; Saint, C. Kinetic study and equilibrium isotherm analysis of Congo Red adsorption by clay materials. *Chem. Eng. J.* **2009**, *148*, 354–364. [CrossRef]
63. Inbaraj, B.S.; Chen, B.H. Dye adsorption characteristics of magnetite nanoparticles coated with a biopolymer poly(γ-glutamic acid). *Bioresour. Technol.* **2011**, *102*, 8868–8876. [CrossRef]
64. Inbaraj, B.S.; Sridhar, K.; Chen, B.H. Removal of polycyclic aromatic hydrocarbons from water by magnetic activated carbon nanocomposite from green tea waste. *J. Hazard. Mater.* **2021**, *415*, 125701. [CrossRef]
65. Langmuir, I. The adsorption of gases on plane surfaces of glass, mica and platinum. *J. Am. Chem. Soc.* **1918**, *40*, 1361–1403. [CrossRef]
66. Girods, P.; Dufour, A.; Fierro, V.; Rogaume, Y.; Rogaume, C.; Zoulalian, A.; Celzard, A. Activated carbons prepared from wood particleboard wastes: Characterisation and phenol adsorption capacities. *J. Hazard. Mater.* **2009**, *166*, 491–501. [CrossRef] [PubMed]
67. Foo, K.Y.; Hameed, B.H. Insights into the modeling of adsorption isotherm systems. *Chem. Eng. J.* **2010**, *156*, 2–10. [CrossRef]
68. Osol, A.; Hoover, J.E. (Eds.) *Remington's Pharmaceutical Sciences*, 15th ed.; Mack Publishing Co.: Easton, PA, USA, 1975.
69. Jaroniec, M.; Deryło, A. Application of Dubinin—Radushkevich—type equation for describing bisolute adsorption from dilute aqueous solutions on activated carbon. *J. Colloid Interface Sci.* **1981**, *84*, 191–195. [CrossRef]
70. Stoeckli, F.; López-Ramón, M.V.; Moreno-Castilla, C. Adsorption of phenolic compounds from aqueous solutions, by activated carbons, described by the dubinin-Astakhov equation. *Langmuir* **2001**, *17*, 3301–3306. [CrossRef]
71. Malana, M.A.; Qureshi, R.B.; Ashiq, M.N. Adsorption Studies of Arsenic on Nano Aluminium Doped Manganese Copper Ferrite Polymer (MA, VA, AA) Composite: Kinetics and Mechanism. *Chem. Eng. J.* **2011**, *172*, 721–727. [CrossRef]
72. Keren, Y.; Borisover, M.; Bukhanovsky, N. Sorption interactions of organic compounds with soils affected by agricultural olive mill wastewater. *Chemosphere* **2015**, *138*, 462–468. [CrossRef]
73. Chatterjee, S.; Guha, N.; Krishnan, S.; Singh, A.K.; Mathur, P.; Rai, D.K. Selective and Recyclable Congo Red Dye Adsorption by Spherical Fe3O4 Nanoparticles Functionalized with 1,2,4,5-Benzenetetracarboxylic Acid. *Sci. Rep.* **2020**, *10*, 111. [CrossRef]
74. Wen, K.; Li, Y.; Zhang, S.; Zhang, X.; Han, R. Adsorption of congo red from solution by iron doped PVA-chitosan composite film. *Desalin. Water Treat.* **2020**, *187*, 378–389. [CrossRef]

75. Liu, J.; Wang, N.; Zhang, H.; Baeyens, J. Adsorption of Congo red dye on $Fe_xCo_{3-x}O_4$ nanoparticles. *J. Environ. Manag.* **2019**, *238*, 473–483. [CrossRef]
76. Munagapati, V.S.; Kim, D.S. Equilibrium isotherms, kinetics, and thermodynamics studies for congo red adsorption using calcium alginate beads impregnated with nano-goethite. *Ecotoxicol. Environ. Saf.* **2017**, *141*, 226–234. [CrossRef] [PubMed]
77. Zourou, A.; Ntziouni, A.; Adamopoulos, N.; Roman, T.; Zhang, F.; Terrones, M.; Kordatos, K. Graphene oxide-$CuFe_2O_4$ nanohybrid material as an adsorbent of Congo red dye. *Carbon Trends* **2022**, *7*, 100147. [CrossRef]
78. Adesina, A.O.; Elvis, O.A.; Mohallem, N.D.S.; Olusegun, S.J. Adsorption of Methylene blue and Congo red from aqueous solution using synthesized alumina–zirconia composite. *Environ. Technol.* **2021**, *42*, 1061–1070. [CrossRef] [PubMed]
79. Hamd, A.; Rady, D.; Shaban, M.; Elsayed, K.N.M.; Al Mohamadi, H.; Elzanaty, A.M.; Ahmed, S.A.; El-Sayed, R.; Soliman, N.K. Application of Nano Bio-clay Composite in a Scaling-up Study for Wastewater Treatment. *Biointerface Res. Appl. Chem.* **2021**, *12*, 6393–6414. [CrossRef]
80. Barany, S.; Strelko, V. Laws and mechanism of adsorption of cations by different ion-exchange forms of silica gel. *Adsorption* **2013**, *19*, 769–776. [CrossRef]